Optimal Control for Bouncing Suppression of CNG Injectors

D. Dyntar

L. Guzzella

Swiss Federal Institute of Technology (ETH),
Zurich, Switzerland

This paper describes the model-based design and the experimental validation of a control system which suppresses the bouncing behavior of Compressed Natural Gas (CNG) fuel injectors. First a detailed model of the system is developed, including temperature and supply-voltage variation effects. Using an optical position sensor, this model is experimentally validated in a second step. Based on this model a feed-forward controller is developed and tested which minimizes the bouncing energy of the system. Since in series applications position sensing would be too expensive to use, an observer-based iterative control algorithm is derived which uses coil current measurements instead of the position information to asymptotically suppress bouncing. [DOI: 10.1115/1.1648311]

1 Introduction

Compressed Natural Gas has several attractive properties when used as a fuel for automotive applications. Its outstanding carbon-to-hydrogen ratio is approximately 1:4 compared to approximately 1:2 for regular gasoline or Diesel fuel. The resulting carbon dioxide emissions thus are substantially lower as well. Moreover, CNG has a relatively high octane number (*RON* 125 or higher, versus *RON* 90 . . . 95 in regular gasoline) which permits higher compression ratios and hence better thermodynamic efficiency levels [1]. Pollutant emissions of CNG engines are also extremely low and thus easily stay within the most severe limits set by emission legislations [2]. Finally, natural gas reserves (including nonstandard sources like methane hydrates) are estimated to be several orders of magnitude larger than those of crude oil [3].

The only serious drawbacks of CNG as a fuel for automotive applications are the slightly reduced volumetric efficiency of the engine, the relatively low energy density of CNG tanks (approximately one half of the value of gasoline), and the as yet missing refuelling infrastructure. The reduced volumetric efficiency can be compensated by supercharging which, as a welcome side effect, also improves the engine's thermodynamic efficiency [1]. Regarding CNG tanks with improved energy densities, various approaches are being discussed including novel storage mechanisms which are expected to alleviate this problem in the future.

The precise control of the air/fuel ratio of CNG engines is a very important prerequisite to realizing the benefits mentioned above. Such control loops will need high-quality, but low-cost actuators for the preparation of the air/CNG mixture. Several ideas for radically new approaches for such actuators with high precision and fast response times have been proposed in the literature [4], however, they all depart from well-established manufacturing and system integration approaches used in actual fuel-injection systems. Economically, it is much more attractive to reuse known conventional gasoline fuel injector designs and adapt them to operate with gaseous fuels like CNG than to introduce entirely new technology.

The main problem encountered in adapting the gasoline fuel injector is the bouncing of the injector needle which is due to the very low damping of the gaseous fuel compared to liquid gasoline. This bouncing impedes a precise fuel dosage and limits injector lifetimes. The key idea of the work described in this paper is to use the coil current of the injector to *actively* counteract this bouncing. For economic reasons, no additional sensors may be

used. Therefore, the coil current will be used as an *information source* based on which the needle position can be estimated.

In order to reach the objectives mentioned, the following steps have been taken:

1. System modelling, including models of *undesirable* effects such as battery voltage dependency and temperature dependency of the coil resistance, etc.
2. Realization of a test environment which permits the validation of the models and of the control algorithms, a cornerstone in this step being the development of a suitable position sensor which monitors the position of the injector needle.
3. Model validation, again including the influence of the *undesirable parasitic effects*.
4. Formulation of a meaningful optimization problem, i.e. seeking that current pattern which minimizes the *bouncing energy* and leads to a model-based solution of this problem.
5. Experimental validation of the proposed control algorithm.

2 Injector System Modelling

The mathematical model of the injector valve basically consists of three interconnected subsystems (Fig. 1):

a. **Electric subsystem:** The coil of the electromagnet forms an electric RL circuit which is connected to the battery voltage with a power-switching transistor. The electric subsystem is coupled to the magnetic ring.

b. **Magnetic subsystem:** It consists of the air gap, the magnetic core (coating), and the armature of the magnet. Due to the magnetic flux the force F_M arises in the air gap. The transformation of the magnetic energy into mechanical energy and vice versa occurs in the air gap whose length varies. The magnetic subsystem is coupled with the electric subsystem through the electromotive force u_{EMK}. The electric effects of this feedback are measured and allow either the calculation of the bouncing energy or, if necessary, the reconstruction of the needle position.

c. **Mechanical subsystem:** It consists of the valve needle connected to the plunger and the spring.

2.1 Electric and Magnetic Subsystems. In a ferromagnetic material, the relative permeability $\mu_r(B)$ depends on the applied field $H[A/m]$ and in fact on the past history of the exposure of the material to magnetic fields. Since the modelling of this phenomenon of hysteresis, in which a ferromagnetic material remembers the past fields, is extremely complex it remains an open research problem [5]. Therefore, in the present work the relationship between the applied field $H[A/m]$ and the internal field $B[T]$ for each material in the magnetic ring was measured and then stored in corresponding inverse look-up tables.
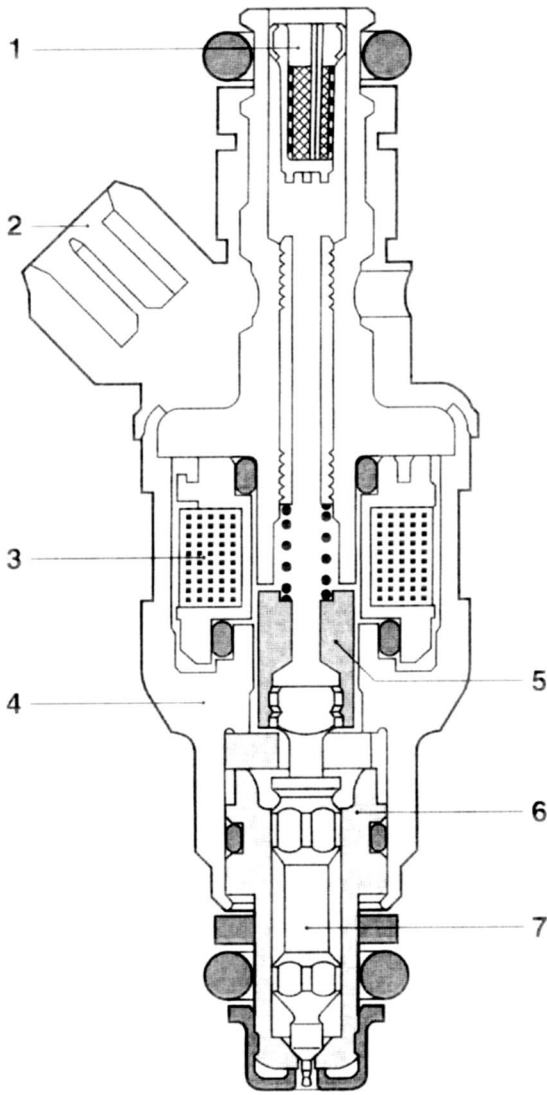
Fig. 1 Cross-section of an injector (courtesy Robert BOSCH GmbH)

Without regard to hysteresis, we receive an unambiguous, non-linear connection between the applied field strength $H[A/m]$ and the flux density $B[T]$. With the relative permeability $\mu_r(B)$ and the permeability of air μ_0 this relationship reads as follows:

$$H = \frac{B}{\mu_0 \cdot \mu_r(B)} \qquad (1)$$

By neglecting the leakage fluxes and the iron losses, we obtain the structure of the model shown in Fig. 2.

The model of the electric subsystem can be written as:

$$u_{batt} = u_c + u_{R_c} = N_{coil} \cdot \frac{d\Phi_M}{dt} + R_c \cdot i_c \qquad (2)$$

The magnetic subsystem (magnetic ring) consists of three different materials and of the air gap. Figure 3 shows the electromagnetic circuit of the injector with the geometrical parameters. Their corresponding reluctance may be computed as follows:

$$R_{m,core} = R_{m,core1} + R_{m,core2} = \frac{l_1 + l_3}{\mu_0 \cdot \mu_{r,core}(B) \cdot A_{core}} \qquad (3)$$

$$R_{m,cas} = R_{m,cas1} + R_{m,cas2} = \frac{l_1 + l_2}{\mu_0 \cdot \mu_{r,cas}(B) \cdot A_{cas}} \qquad (4)$$
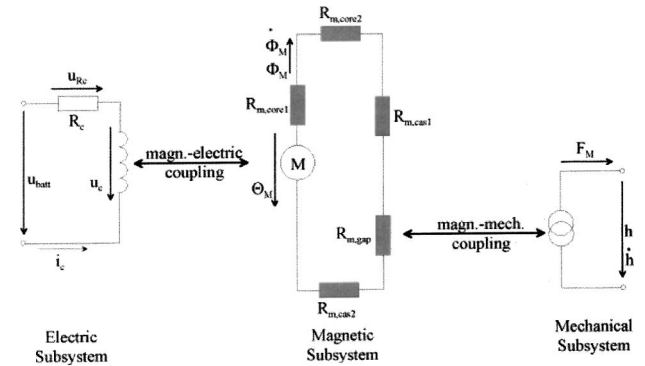
Fig. 2 Model of three connected subsystems of the electromagnet

$$R_{m,plunger} = \frac{l_4}{\mu_0 \cdot \mu_{r,plunger}(B) \cdot A_{plunger}} \qquad (5)$$

The geometry (length) of the air gap in the magnetic ring varies as a function of the position h of the plunger which is connected with the valve needle.

$$R_{m,gap} = \frac{h}{\mu_0 \cdot A_{gap}} \qquad (6)$$

From the known reluctance and magnetic flux Φ_M the magnetic flooding Θ_M as well as the current in the coil can now be computed:

$$\Theta_M = \Phi_M \cdot \sum_\nu R_{m,\nu}, \quad i = \frac{\Theta_M}{N_{coil}} \qquad (7)$$

The calculation of the magnetic force F_M of the valve solenoid can be carried out on the principle of virtual displacement. Any change dh in the displacement of the magnetic air gap causes the following mechanical work W_{mec} to be performed:

$$dW_{mec} = F_M \cdot dh \qquad (8)$$

Based on the energy density, the decrease of the magnetic energy W_{mag} due to the volume reduction of the magnetic air gap in the direction of the plunger shift h can be computed as follows:
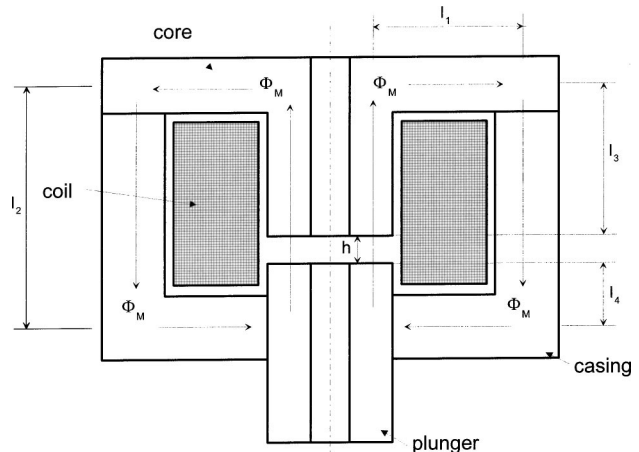

Fig. 3 Sectional view of the electromagnetic circuit

$$dW_{mag} = d\left\{\frac{B^2 \cdot A_{\text{plunger}} \cdot h}{2 \cdot \mu_0}\right\} = d\left\{\frac{\Phi_M^2 \cdot h}{2 \cdot \mu_0 \cdot A_{\text{plunger}}}\right\}$$
$$= dW_{mec} = F_M \cdot dh \qquad (9)$$

A_{plunger} .. square of the air gap $[m^2]$

Finally, the magnetic force is obtained as follows:

$$F_M = \frac{\Phi_M^2}{2 \cdot \mu_0 \cdot A_{\text{plunger}}} \qquad (10)$$

2.2 Mechanical Subsystem. The valve needle is influenced by the following additional forces:

a. The spring force F_f with pre-tension $F_{f,0}$ end the spring constant k_C, f can be calculated as follows: $F_f = k_{Cf} \cdot h + F_{f,0}$

b. The gas pressure p_{gas} causes a gas force F_{gas}. Due to the complex shape of the inner part of the valve and the complex supersonic gas flow behavior [6], it is possible but a rather complex task to calculate this gas force exactly. However, it is obvious that it is not needed to calculate the behavior of the mechanical and pneumatic phenomena more accurately, because the debouncing control algorithm is running in closed loop and, better yet, in real time. In addition, since the gas pressure in the rail is regulated, the pressure changes amount to less than 2% of the set point (usually set point is 8,000 HPa). Therefore, this force was measured and assumed to be constant at the operating point.

$$F_{gas} = p_{gas} \cdot k_{gas}, \quad k_{gas} = 0.82[N \cdot bar^{-1}] \qquad (11)$$

c. Friction and damping forces are modelled as the constant k_d as shown in Eq. (12).

d. The force of gravity of the valve needle is neglected.

The sum of all these forces accelerates the valve needle:

$$(m_{needle} + m_{\text{plunger}}) \cdot \frac{d^2h}{dt^2} = F_M - k_d \cdot \frac{dh}{dt} - k_{Cf} \cdot h - F_{f,0} - F_{gas} \qquad (12)$$

Another difficult problem is modelling the impact behavior of the valve needle at the upper and lower mechanical limits. This impact behavior is highly nonlinear and discontinuous. For a simple but sufficiently precise model, we assume a sign reversal and a simultaneous decrease of the needle velocity at the time of the impact. With the coefficient of restitution k_{res} this relationship reads as follows:

$$\nu(t_+) = -sign[\nu(t_-)] \cdot |\nu(t_-)| \cdot k_{res}, \quad 0 < k_{res} < 1 \qquad (13)$$

2.3 Observer of the Valve Temperature. A simple observer calculates the temperature ϑ_{coil} of the electromagnetic coil from the coil current $i_{c,ss}$ and from the battery voltage $u_{batt,ss}$, both at steady state, with the valve completely open:

$$\vartheta_{coil} = k_{cu} \cdot \frac{u_{batt,ss}}{i_{c,ss}}, \quad k_{cu} \ldots [K \cdot \Omega^{-1}] \qquad (14)$$

3 Experimental Setup and Model Validation

3.1 Test Bench and Position Sensor. The behavior of the injector was first examined while the injector was removed from the engine. For the measurement of the valve position an optical sensor with a bandwidth of 100 kHz was developed (see Fig. 4).

Once the injector is built into the engine, the needle position of the valve cannot be measured directly with an optical sensor. Therefore, an observer-based iterative control algorithm is derived which asymptotically suppresses bouncing using measurements of the coil current instead. Unfortunately, with a standard power amplifier stage there is no current flow through the magnetic coil while the valve is closing and therefore the position of the injector needle cannot be reconstructed. A special power amplifier stage has been developed, which guarantees that in every operating state of the injector a specific current flows through the electromagnetic
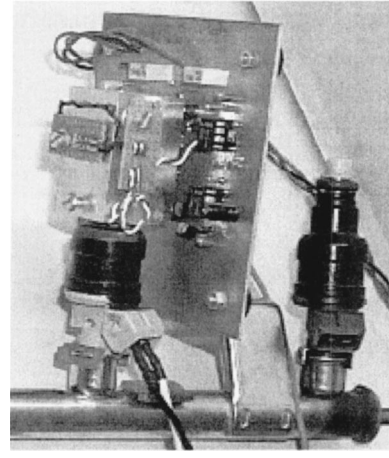

Fig. 4 Test bench with optical position sensor for the investigation of the injector behavior used for parameter identification

coil, even while the valve is closing. The position of the valve needle can be thus reconstructed from the measured current.

Figure 5 shows the comparison between predicted and measured system behaviors after the battery voltage is switched on. Such perfect results can be obtained under the condition that the model parameters have been identified very exactly in the chosen operating point. However, in a real application this will hardly be the case and the use of an observer or another adaptation method is necessary.
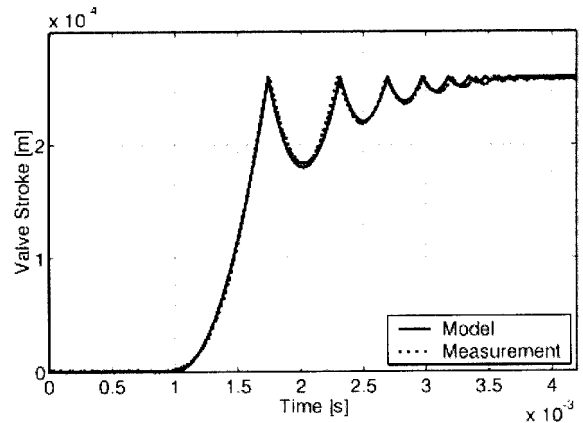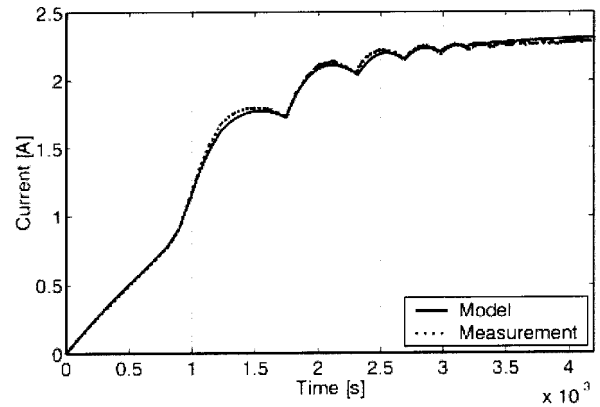

Fig. 5 Comparison between predicted and measured system behaviors after battery voltage is switched on. Operating point: p_{gas}=9.3 bar, u_{batt}=12 V, R_{coil}=5.3 Ω.
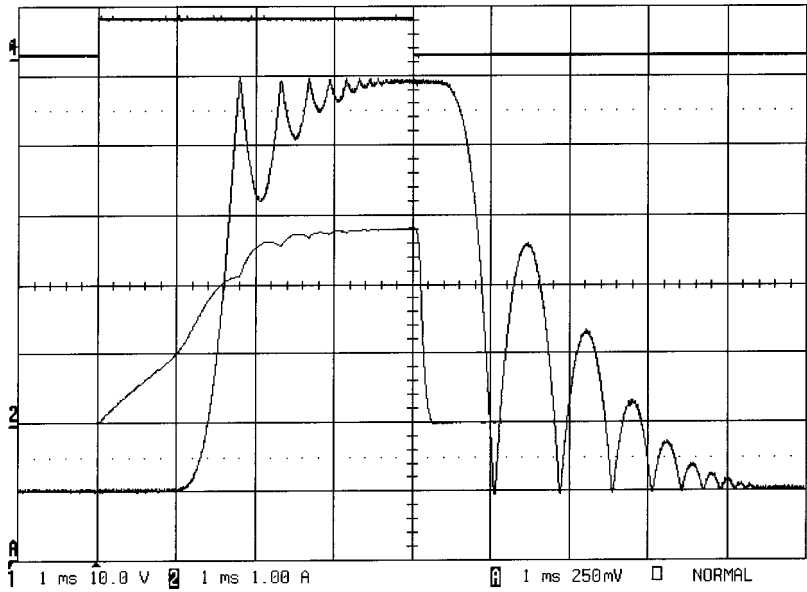
Fig. 6 Switch-on and switch-off transients with typical bounce effects without bouncing suppression (Ch1.. Electronic Engine Control Unit-Pulse, Ch2.. i_c [1 A/div], ChA.. Needle position [0.05 mm/div], Time.. [1 ms/div])

For the debouncing control strategy shown in this paper, the position of the valve needle does not need to be reconstructed. The calculation of the bouncing energy from the measured coil current in real time is entirely sufficient.

4 Optimal Control of Bouncing Energy

4.1 Problem Formulation. The bouncing of the injector needle (see Fig. 6) negatively affects the behavior of the natural-gas engine, because of stochastic effects and system nonlinearities in the mass throughput of the natural gas. In addition, the bouncing shortens the lifespan of the injection valves.

Figure 6 shows the behavior of a not debounced injector with typical switch-on and switch-off transients. The switch-off bouncing is twice as strong as the switch-on bouncing because the mag-

netic force of the valve solenoid $F_M = 0$ and the valve needle is forced to the lower mechanical limit by the force of the spring and the gas force only.

While the engine is running, the permanently changing environmental variables of the injector such as natural gas pressure in the rail, battery voltage, and operating temperature critically influence the bouncing behavior. Any real-time debouncing closed-loop control strategy that is to substantially reduce or even eliminate this bouncing, even if the environmental variables are changing, has to take these effects into consideration.

4.2 Solution. As shown in Fig. 7, the debouncing control strategy of the injector needle is implemented by well-aimed brake pulses. An optimization algorithm controls the position t_p and the pulse width t_b of each brake pulse, with the result that the
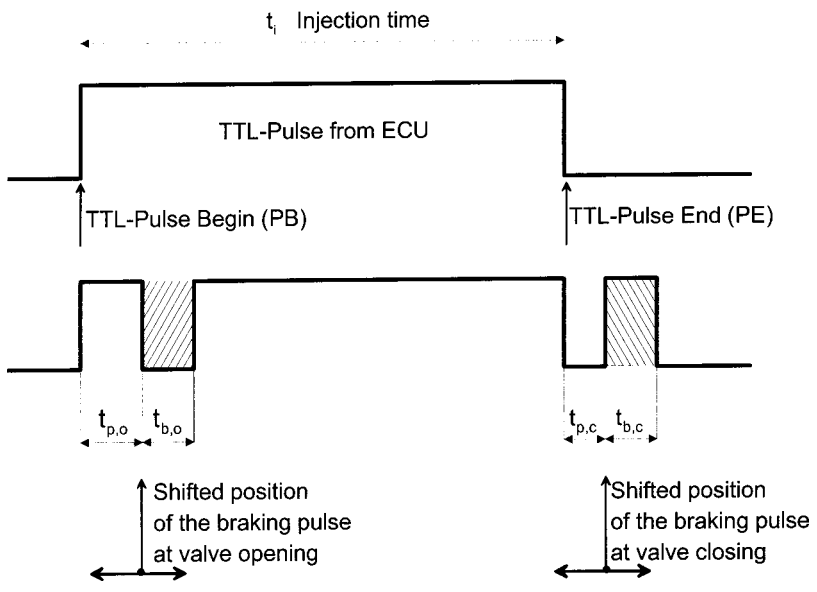

Fig. 7 Position and width of the braking pulses as shifted by the optimization algorithm. (Index $t_{.,o}$ for opening and $t_{.,c}$ for closing)
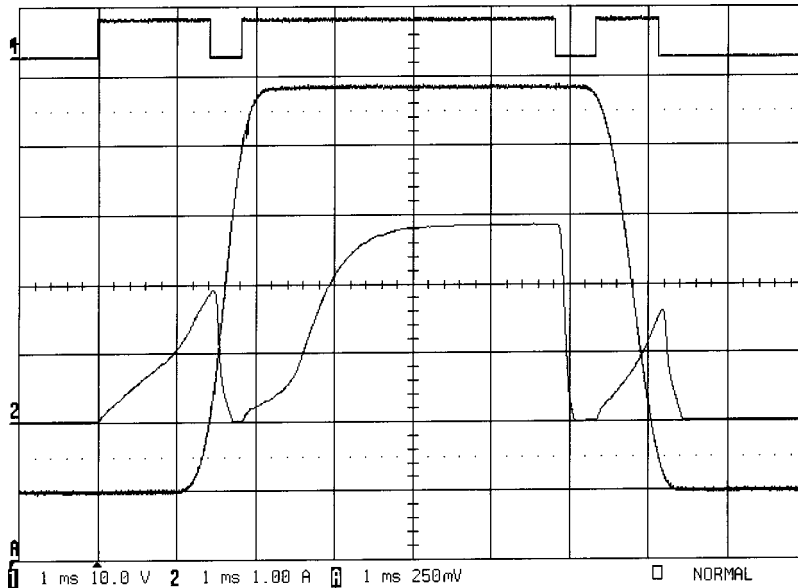
Fig. 8 Switch-on and switch-off transients with proposed optimal bouncing suppression (Ch1.. Optimal pulse pattern, Ch2.. i_c [1 A/div], ChA.. Needle position [0.05 mm/div]

bouncing energy $W(t_p,t_b,k)$ is minimized. At the time position $t_{p,o}$, the battery voltage is switched off for a short time $t_{b,o}$. At pulse end, i.e., at the time position $t_{p,c}$, the battery voltage is switched on for a short time $t_{b,c}$. If these brake pulses are of the optimal width and occur at the optimal time position, the injector needle is decelerated such that it reaches the upper or lower mechanical stop with zero velocity, as shown in Fig. 8.

4.3 Definition of Bouncing Energy. The cost function for the optimization is the bouncing energy $W(k)$ of the injector needle at the engine cycle k. It can be calculated either directly from the measurement of the position h (if available),

$$W_h(t_p,t_b,k)=k_h\int_0^{t_{EP}}h^2(\tau)\cdot d\tau\bigg|_{(k)} \tag{15}$$

or indirectly from the reconstructed position h_r based on the measured coil current i_c while the injector needle is bouncing.

$$W(t_p,t_b,k)=k_{h_r}\int_0^{t_{EP}}h_r^2(\tau)\cdot d\tau\bigg|_{(k)} \tag{16}$$

The bouncing energy cost function $W(t_p,t_b,k)$ has multiple local minima. Therefore it is necessary at each operating point to bracket the suitable convex interval. The independent variables t_p and t_b will than be calculated as follows (see Fig. 9):

$$t_p=t_{p,b}+\Delta t_p \tag{17}$$

$$t_b=t_{b,b}+\Delta t_b \tag{18}$$

The rough base values $t_{p,b}$ and $t_{b,b}$ are stored in a look-up table for different operating points. These base values lead the optimization algorithm into the direct convex proximity of the corresponding global minimum. The fine-tuning of the values t_p and t_b then is a result of the values Δt_p and Δt_b, which are calculated at each new engine cycle by the optimization algorithm. This feed-forward control strategy keeps the number of iterations to a minimum, which increases the real-time efficiency of the optimization algorithm.

While operating in the engine, the injector is switched on and off with the frequency of the engine duty-cycle. In each cycle, the position of the injector valve is reconstructed from the measured coil current. Subsequently the bouncing energy is determined and
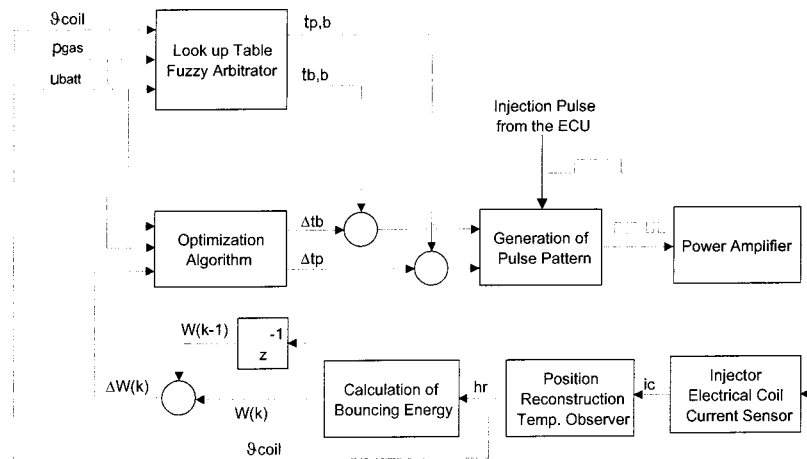

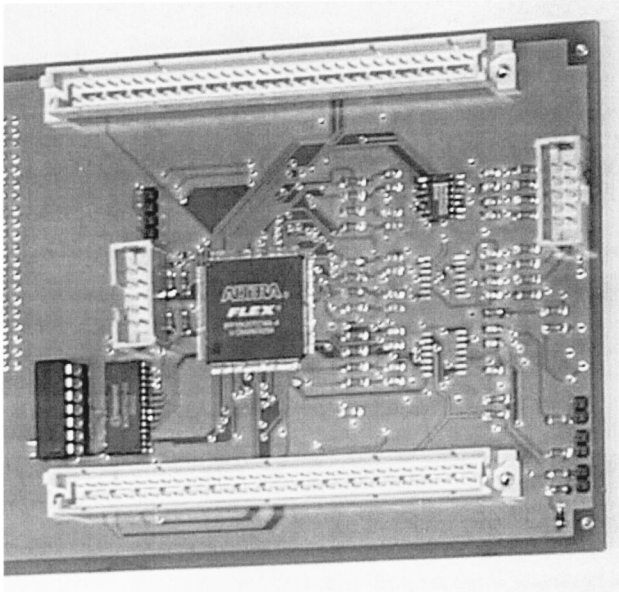**Fig. 9 Diagram of the optimization**

Fig. 10 Test board with the FPGA chip and $\Sigma-\delta-$A/D converter circuits
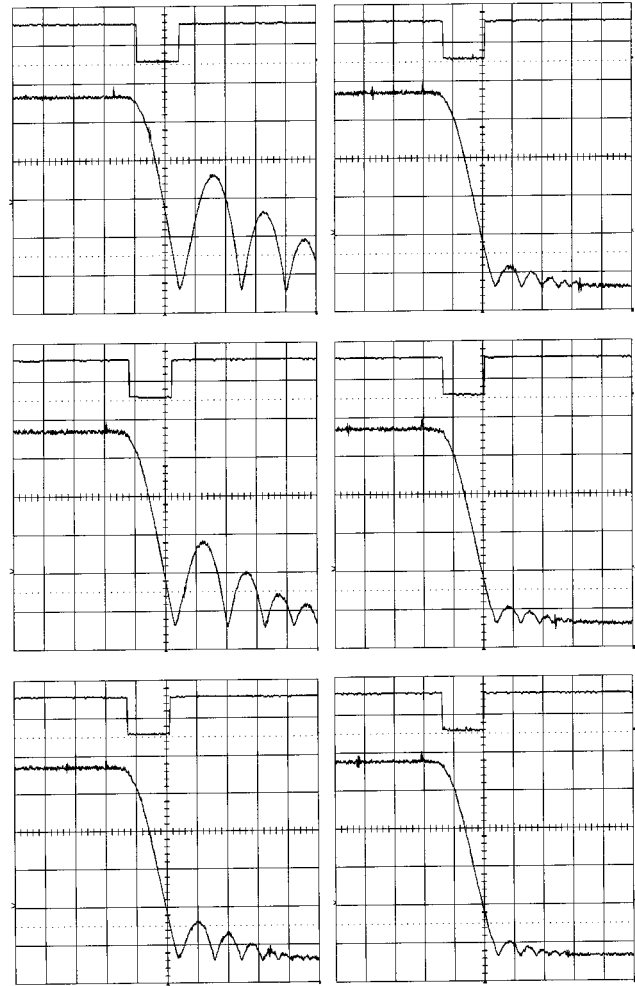

Fig. 11 The first six measurements of the control algorithm during the de-bouncing process at a sampling frequency of 25 Hz (3000 rpm). Scaling: Brake pulse (upper curve) 5 V/div, Injector needle position (lower curve) 0.05 mm/div, time 0.5 ms/div

then the optimization algorithm calculates the new position and width of the brake pulse. Finally, the new improved pulse pattern is generated, which decreases the bouncing energy for the following engine cycle. This real-time strategy continuously minimizes the bouncing energy (see Fig. 11).

5 Current-Based Control

5.1 Control Algorithm. As described in Sec. 4.2, position and width of the braking pulses are calculated by a 2-D optimization algorithm.

From any a particular starting point $\mathbf{y}_0$ which is defined as the origin of the two-dimensional coordinate system with coordinates $\mathbf{y}=[t_p,t_b]$, the bouncing energy function $W(t_p,t_b)$ can be approximated by its Taylor series:

$$W(\mathbf{y})=W(t_p,t_b)=W(\mathbf{y}_0)+\frac{\partial W(t_p,t_b)}{\partial t_p}\cdot t_p+\frac{\partial W(t_p,t_b)}{\partial t_b}\cdot t_b$$
$$+\frac{1}{2}\left\{\frac{\partial W^2(t_p,t_b)}{\partial t_p\partial t_b}\cdot t_pt_b+\ldots\right\} \quad (19)$$

$$W(\mathbf{y})\approx W(\mathbf{y}_0)+\nabla W(\mathbf{y})^t\mathbf{y}+\frac{1}{2}\mathbf{y}^tH\mathbf{y} \quad (20)$$

Assuming that the inverse of the Hessian matrix H exists, then with Newton's method each successor point $\mathbf{y}_{k+1}$ is given by:

$$\mathbf{y}_{k+1}=\mathbf{y}_k-H(\mathbf{y}_k)^{-1}\nabla W(\mathbf{y}_k) \quad (21)$$

In the present work, the variable-metric *Davidon-Fletcher-Powell (DFP)* method for optimization is used [7]. The cost function $W(t_p,t_b)$ can be locally approximated by the quadratic form of Eq. (20). With successive line minimizations of the quadratic cost function along conjugate directions, one pass of two line minimizations should bring it exactly to the minimum. However, since the cost function $W(t_p,t_b)$ is not exactly quadratic, this will not be the case in general.

With the *DFP method* the search directions are of the form $\mathbf{d}_j=-C_j\nabla W(\mathbf{y})$, in lieu of $\mathbf{d}_j=-H_j^{-1}\nabla W(\mathbf{y})$, as in Newton's method. The *DFP method* eliminates the need of multiple measurements followed by the calculation of second derivatives,

because the inverse of the Hessian Matrix H^{-1} is approximated by the positive definite, symmetric matrix C, which is determined by successive calculations without knowledge of second derivatives:

$$C_{j+1}=C_j+\frac{\mathbf{p}_j\mathbf{p}_j^t}{\mathbf{p}_j^t\mathbf{p}_j}-K_j \quad (22)$$

where the Davidon correction matrix is

$$K_j=\frac{C_j\mathbf{q}_j\mathbf{q}_j^tC_j}{\mathbf{q}_j^tC_j\mathbf{q}_j} \quad (23)$$

and with the optimal solution of the 1-D optimization λ^*

$$\mathbf{p}_j=\lambda_j^*\mathbf{d}_j\equiv\mathbf{y}_{j+1}-\mathbf{y}_j \quad (24)$$

$$\mathbf{q}_j=\nabla W(\mathbf{y}_{j+1})-\nabla W(\mathbf{y}_j) \quad (25)$$

5.2 Iterative Optimization Algorithm.

1. *Preinitialization step*: Set the termination scalar $\varepsilon>0$. Read the initial point $\mathbf{x}_1$ from the look-up table and set $C=I$. Let $\mathbf{y}_j=\mathbf{x}_I$, let $k=j=1$, and go to the next step.
2. *Optimization step*: If $\|\nabla W(\mathbf{y}_j)\|<\varepsilon$, go to the reinitialization step; else, let $d_j=-C_j\nabla W(\mathbf{y}_j)$ and let λ_j be an optimal

solution of the 1-D optimization which minimizes $W(\mathbf{y}_j + \lambda_j \mathbf{d}_j)$.

Let $\mathbf{y}_{j+1} = \mathbf{y}_j + \lambda_j^* \mathbf{d}_j$. If $j < 2$, construct C_{j+1} from Eq. (22), replace j by $j+1$, and repeat the optimization step.

If $j = 2$, let $\mathbf{y}_1 = \mathbf{x}_{k+1} = \mathbf{y}_3$, replace k by $k+1$, let $j = 1$, and repeat the optimization step.

3. *Reinitialization step*: Set $C = I$, let $k = j = 1$, and go to the optimization step 2.

This iterative optimization algorithm is interrupted by a fuzzy decision algorithm with feed-forward control which is running in a concurrent process whenever the operating point of the injector changes. After the interruption the optimization algorithm returns to the preinitialization step.

For an increase of the real-time efficiency, a 1-D optimization algorithm can be used after the starting and warm-up periods. In this case, just the position of the brake pulse is changed. However, the width of the brake pulse remains fixed during the optimization.

6 System Test

The optimization algorithm described above has been implemented on a Field Programmable Gate Array (FPGA) board (see Fig. 10) using the hardware description language VHDL. This technology allows the truly concurrent calculation of all eight optimization algorithms (in the case of a four-cylinder engine with one each switch-on and switch-off optimization algorithm per cylinder), including the acquisition at 100 kHz of the four injector coil currents, four injector coil temperatures, battery voltage, and gas pressure.

The results of a typical change in operating point are shown in Fig. 11.

The first graph in the left column shows the bouncing transient immediately after a reinitialization effected because the operating point of the valve (for instance the battery voltage) has rapidly changed. The optimization algorithm resides in the proximity of the optimum in which the convex bouncing energy is minimal. The graph clearly shows the position of the braking pulse. The second graph in the left-hand column shows the bouncing transient after the first optimization step. The position of the braking pulse was shifted to the left by about 100 microseconds, which reduced the bouncing. Finally, in the sixth step, the position of the braking pulse is almost optimal and the bouncing is insignificant.

7 Conclusion

A nonlinear control strategy for CNG injectors is presented. The first part describes and models the electromagnetic injection valve for compressed natural gas, as well as its bouncing behavior. The second part derives a control strategy for the elimination of the undesirable bouncing effects of the injector needle.

The proposed real-time control algorithm minimizes the undesirable bouncing of the CNG injectors. Since any position sensing of the injector needle in production-type vehicles would be too expensive and therefore is not available, an observer-based iterative closed-loop control algorithm has been derived which asymptotically suppresses bouncing using coil current measurements instead of the position information.

The optimization algorithm was implemented on a *Field Programmable Gate Array* (FPGA) board and has been successfully tested in the CNG engine of a four-cylinder engine (A4, 1.8l, 20V).

References

[1] Heywood, J. B. 1988, *Internal Combustion Engine Fundamentals*, McGraw-Hill, New York.

[2] California Certification Exhaust Emission Standards, US Environmental Protection Agency, 2000, Office of Transportation and Air Quality, EPA420-B-00-001 February.

[3] Holder, G. D., Kamath, V. A., and Godbole, S. P., "The potential of natural gas hydrates as an energy resource," Ann. Rev. Energy, **9**, 427.

[4] Favrat, D., Germano, S., and Nicollerate, M., Ultra Rapid Natural Gas Port Injection, SAE 951913.

[5] Mayergoyz, I. D., Adly, A. A., and Friedmann, G., 1990, Appl. Phys., **5**, 67.

[6] Rist D., 1996, Dynamik realer Gase, Springer, Berlin, New York.

[7] Jacobs, D. A. H. (ed.) 1997, The State of the Art in Numerical Analysis (London: Academic Press), Chapter 111.1 §§3-6 (by K. W. Brodlie).